Modification of divertor heat and particle flux profiles with applied 3D fields in NSTX H-mode plasmas

Modification of divertor heat and particle flux profiles with applied 3D fields in NSTX H-mode plasmas

J.-W. Ahn[1,a], J.M. Canik[1], V.A. Soukhanovskii[2], R. Maingi[1] and D.J. Battaglia[1]

[1] Oak Ridge National Laboratory, Bethel Valley Road, Oak Ridge, TN 37831, USA
[2] Lawrence Livermore National Laboratory, 7000 East Ave., Livermore, CA 94551, USA

E-mail: jahn@pppl.gov

Abstract
Externally imposed non-axisymmetric magnetic perturbations are observed to alter divertor heat and particle flux profiles in the National Spherical Torus Experiment (NSTX). The divertor profiles are found to have a modest level of multiple local peaks, characteristic of strike point splitting or the 'magnetic lobe' structure, even before the application of the 3D fields in some (but not all) NSTX discharges. This is thought to be due to the intrinsic error fields. The applied 3D fields augmented the intrinsic strike point splitting, making the amplitude of local peaks and valleys larger in the divertor profile and striations at the divertor surface brighter. The measured heat flux profile shows that the radial location and spacing of the striations are qualitatively consistent with a vacuum field tracing calculation. 3D field application did not change the peak divertor heat and particle fluxes at the toroidal location of measurement. Spatial characteristics of the observed patterns are also reported in the paper.

(Some figures in this article are in colour only in the electronic version)

1. Introduction

The application of small, 3D magnetic field perturbations produced by internal or external coils has been found to have a significant impact on the plasma performance in tokamaks. As the present plan for the International Thermonuclear Experimental Reactor (ITER) relies on the use of non-axisymmetric magnetic perturbation for the edge localized mode (ELM) suppression [1], the effect of these 3D fields on the heat and particle footprints on the divertor plates is of considerable interest.

While ELMs are a threat to the integrity of plasma facing components because of their large transient heat flux, the ELM-free operation results in continuous impurity buildup in the core plasma in high confinement mode or 'H-mode' (in the absence of other cross field transport enhancements). This could be especially important in spherical tori, where it has been predicted that, due to the strong shaping and low aspect ratio, extremely high pedestal pressures may be achieved before ELM stability limits are reached [2]. In DIII-D [3],

large type-I ELMs have been successfully eliminated [4–7] by applying resonant magnetic perturbations (RMPs) produced by a series of coils inside the vacuum vessel (internal or 'I-coils'). In the National Spherical Torus Experiment (NSTX) [8], long ELM-free H-mode plasmas were achieved by heavy lithium evaporation and coating onto the plasma facing components [9]. Application of 3D fields to these plasmas triggered ELMs to flush impurities [10, 11] with the ELM frequency controlled by the frequency of applied 3D field coil currents.

When the external 3D field is applied, modification of the magnetic equilibrium produces a 3D structure of perturbed magnetic field lines in the plasma edge, where the poloidal magnetic flux is re-organized into topological structures known as homoclinic tangles [12]. Perturbed by non-axisymmetric 3D fields, the separatrix is split into multiple invariant manifolds forming a 3D 'lobe' structure for the open field lines, which are a mixture of long connection length stochastic field lines and short connection length laminar field lines. The lobe structure of the open field lines generates a striated strike point pattern radially across the divertor target surface. This structure is expected to be reflected in the measured divertor heat and particle flux profiles, due to the

[a] Author to whom any correspondence should be addressed. Princeton Plasma Physics Laboratory, MS-15, Princeton, NJ 08543, USA.
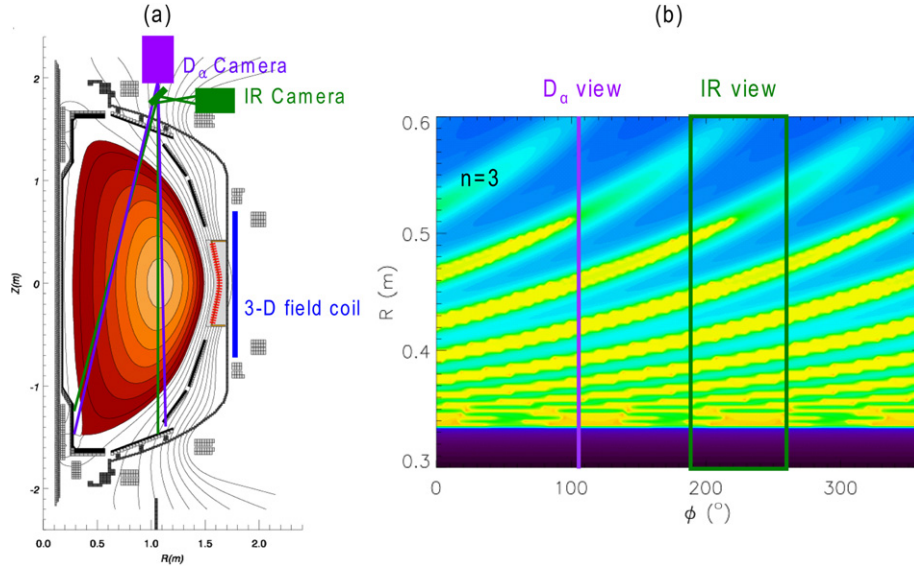
Figure 1. Schematic view of the poloidal cross section of NSTX (*a*) with magnetic equilibrium reconstruction, field of view of the IR and D_α cameras and the location of external 3D field coil overlaid. Figure (*b*) shows the contour plot of calculated connection lengths for $n = 3$ application, showing the formation of the lobe structure as a function of toroidal angle (φ) and radius. The spatial coverage of D_α and IR cameras is also shown.

rapid parallel transport along the open field lines. Indeed, such an observation during the RMP application was recently reported [13] in DIII-D H-mode discharges. This result shows the formation of a striated strike point pattern for heat flux for high (>0.5) pedestal electron collisionality, $\nu_e^* = q_{95} R \varepsilon^{-3/2} \lambda_{ee}^{-1}$, while particle flux showed striation for both high and low collisionalities. Here, R is the major radius, ε is the inverse aspect ratio ($\varepsilon = a/R$) and λ_{ee} is the electron mean free path.

A high speed infrared (IR) camera was newly implemented [14] on NSTX, enabling measurement of the heat flux profiles during the application of a 3D magnetic field. A 1D CCD array also views the divertor plates to obtain D_α profiles [19]. This paper also reports the signatures of the magnetic lobe structure in the heat flux and D_α profiles in NSTX H-mode plasmas, as well as the effect of coil current variation on the observed lobe characteristics. In general, the measured heat flux profile has characteristics expected from the lobe structure and strike point splitting, similar to the DIII-D result at high collisionality [13].

2. Experimental set-up

The effect of 3D perturbative magnetic field was investigated in the low aspect ratio NSTX ($R = 0.85$ m, $a < 0.67$ m, $R/a > 1.27$), where H-mode plasmas are routinely accessed [16] via good wall conditions, auxiliary heating power, flexible plasma position and shape controls. In these experiments, the toroidal magnetic field (B_t) at the magnetic axis was fixed at ~ 0.45 T, and the neutral beam injected power (P_{NBI}) of 4 MW was used. Plasmas were highly shaped (elongation $\kappa \sim 2.4$, triangularity $\delta \sim 0.8$), and the plasma current was fixed at $I_p = 800$ kA. The equilibrium was maintained as a lower single-null but was close to double-null with dr_{sep} (radial separation at the midplane between the primary and secondary separatrices) of ~ 0.5 cm. Also, the direction of the
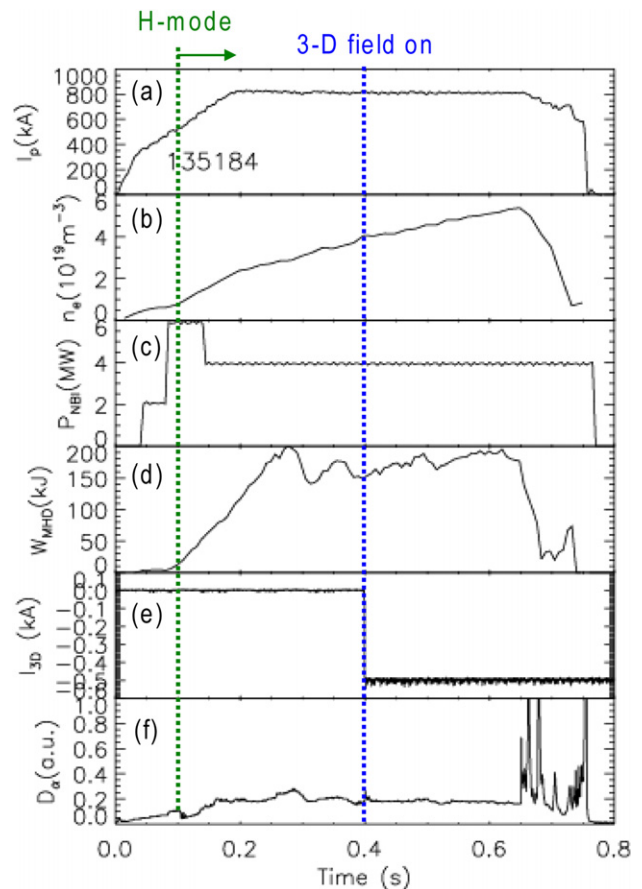

Figure 2. Time evolution of various discharge parameters for a 3D field applied shot 135184: (*a*) plasma current, (*b*) line averaged density, (*c*) injected NBI power, (*d*) total stored energy, (*e*) current in the external 3D coil and (*f*) D_α signal for lower divertor. Note that the 3D field coil was switched on at 400 ms to -0.5 kA and this did not trigger an ELM over the entire 3D field application period.
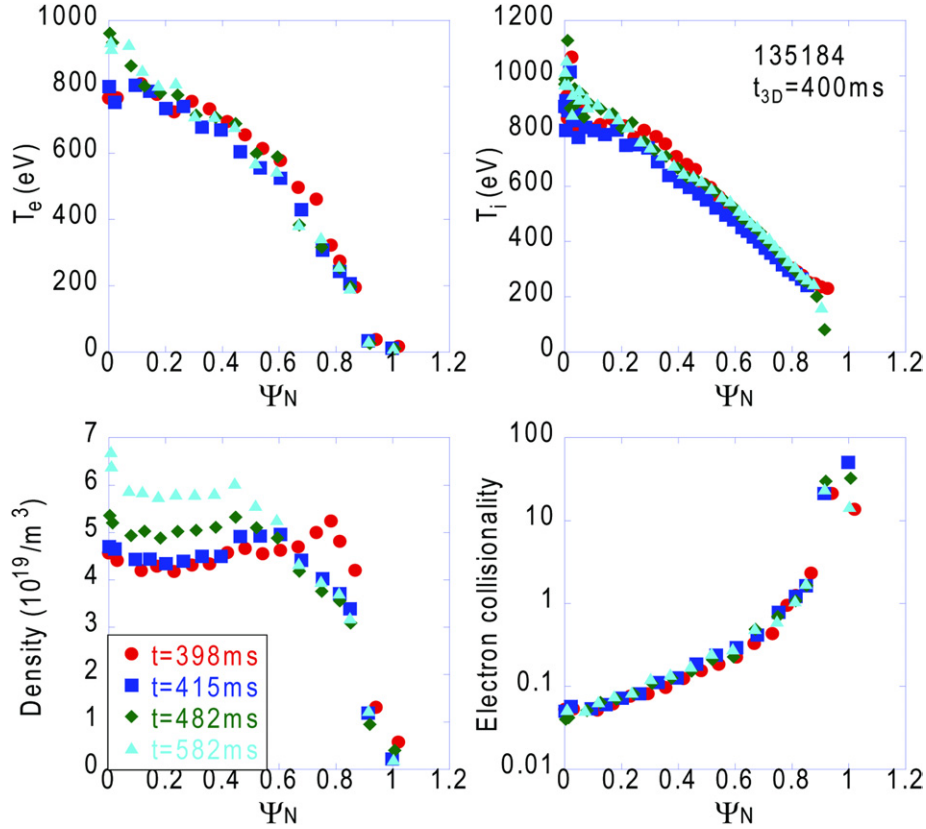
Figure 3. Evolution of plasma profiles across the application of $n = 3$ perturbation fields at $t = 400$ ms over a period of $\sim$200 ms.

B-field was for the ion ∇B drift to move towards the primary X-point. The 3D perturbation fields were generated with a set of six midplane coils, external but close-fitting to the vacuum vessel, that are typically used for error field correction and resistive wall mode feedback control [17, 18]. The coils were configured to apply an $n = 3$ field in the ELM-destabilization experiments, with a generated magnetic perturbation at the separatrix, $\delta B/B = 0.6$–0.7% for the peak δB at the coil centre and in the order of 0.1% for the integrated δB over the coil surface. The poloidal spectrum of the applied magnetic perturbation is broad at the plasma edge, reaching high enough mode numbers to be resonant with high edge safety factor values ($q_{95} \sim 10$).

Figure 1 shows the poloidal cross section of NSTX showing the location of the diagnostic views as well as the external 3D field coil. The magnetic equilibrium for a typical discharge is also overlaid. Also shown in figure 1 is the contour plot of the calculated connection lengths at the divertor surface using a vacuum field line following code with the application of external $n = 3$ fields. The formation of the 3D lobe structure is clearly seen. The spatial coverage of the NSTX D_α (1D) and IR (2D) cameras is also overlaid.

The heat flux measurement is made with an SBF-161 IR camera [14], installed at toroidal angle $\varphi = 225°$. The camera takes IR images of the lower divertor plates in 2D with a temporal resolution of 1.6 to 6.3 kHz (depending on the frame size). The front lens focal length of 25 mm gives a $45°$ of circular field of view (FOV), with $\sim$6.7 mm spatial resolution at the divertor target. The camera measures surface IR emission, which is converted to surface temperature from

bench and *in situ* calibrations. A 2D heat conduction code called THEODOR [15] is used to calculate the divertor heat flux profile from the measured surface temperature. The calculation is carried out in both radial and tile depth directions for tiles with finite thickness as well as taking account of temperature dependent material parameters. The effect of thin layers on the top of the tile surface on the observed IR emissivity is also considered in the code, by introducing the so-called α-parameter in the calculation as a ratio of heat conductivity to the thickness of the layer. The determination of α-parameter is presently made by comparing the estimated energy flowing with the divertor target by the IR measurement with the power balance consideration. However, the effect of Li coatings on the surface emissivity is not properly assessed at present in NSTX and we are working to implement a 2-colour IR system to resolve this issue. Therefore, the heat flux data presented in this paper are not absolutely calibrated, and only the relative comparison should be considered valid. The several kilohertz framing rate is a substantial improvement over the existing 30 Hz frame IR cameras [19], and the improved temporal resolution enables heat flux measurement of transient events, such as ELMs and disruptions. The fast framing rate also facilitates measurement of the formation of the magnetic lobe structure in the heat flux profile, which can start to appear within 3–4 ms after initiation of the 3D field coil.

The D_α emission at the lower divertor target is recorded by a 1D CCD camera installed at $\varphi = 105°$. It is operated at a rate of 2 kHz with sub-millimetre spatial resolution and is a part of the system of CCD arrays that are spectrally filtered for deuterium Balmer-α (656.1 nm), Balmer-γ (433.9 nm)
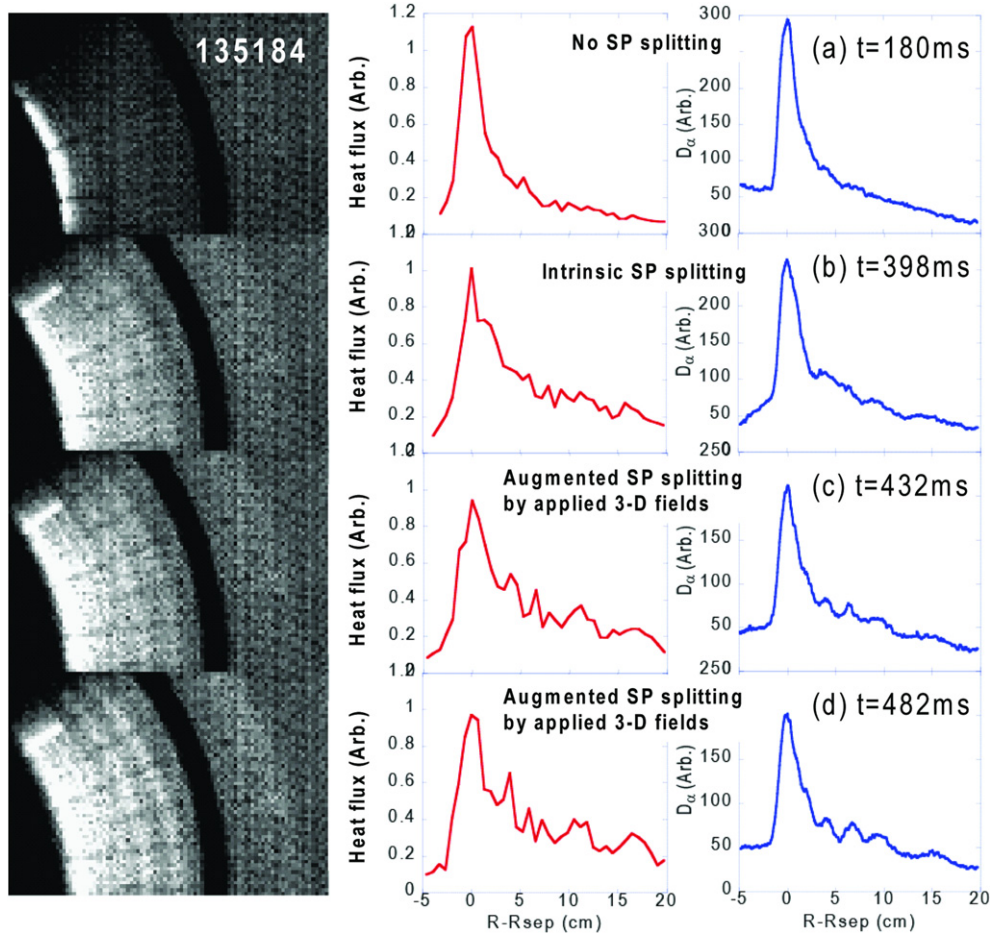
Figure 4. Raw IR images of lower divertor plates from the top of NSTX (left column), measured heat flux (middle), and D_α (right) profiles taken at different time slices for a discharge with $n = 3$ 3D fields applied from $t = 400$ ms, showing (*a*) no strike point (SP) splitting at earlier stage, (*b*) 'intrinsic' SP splitting 2 ms before the 3D field application and (*c*), (*d*) 'augmented' SP splitting by the applied 3D fields.

and/or HeII Paschen-α (468.5 nm) emission lines using $\Delta\lambda =$ 1.0–1.5 nm bandpass interference filters [20]. The D_α emission is closely correlated with the particle flux in attached plasmas, due to its strong dependence on the plasma density.

3. Influence of non-axisymmetric field on heat flux and D_α profiles

The amplitude of the 3D field perturbations was scanned by varying coil currents from 0.5 to 1.0 kA. Lithium wall conditioning/coating was used, provided by two lithium evaporators [21], to produce baseline ELM-free H-mode plasmas. The temporal evolution of a typical discharge is shown in figure 2. The L–H transition is indicated by the drop of divertor D_α emission at $t \sim 105$ ms, and the H-mode was sustained until $t \sim 650$ ms. The 3D field perturbation was applied from 400 ms with constant amplitude of 0.5 kA. The D_α trace shows that the discharge remained ELM-free after the application of the 3D field, while the applied magnetic perturbation did induce ELMs for higher coil currents $I_{3D} \geqslant$ 0.75 kA. The line-average electron density continued to rise in the H-mode phase. Figure 3 shows the profile evolution of the electron temperature (T_e), density (n_e), ion temperature (T_i) and electron collisionality (ν_e^*). Note that the n_e profile
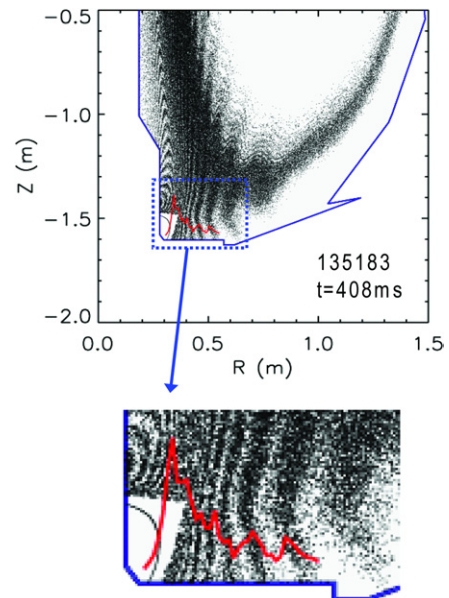

Figure 5. Magnetic footprints on the divertor target, calculated by a vacuum field line tracing code for the toroidal location of the IR camera at $\varphi = 225°$, with the measured heat flux profile overlaid.
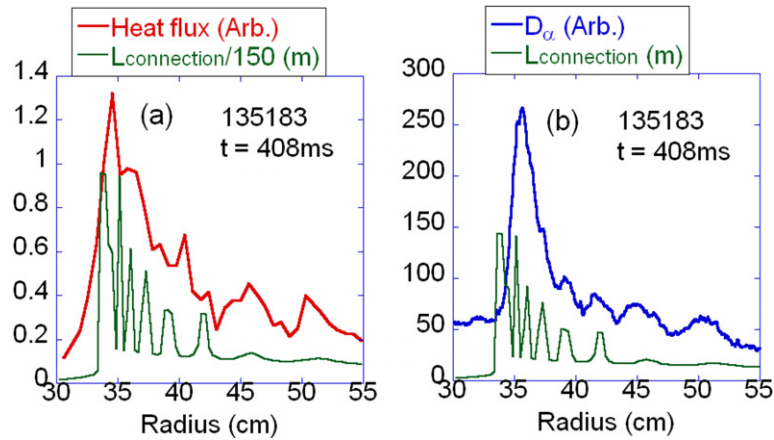
Figure 6. Comparison of (*a*) heat flux and (*b*) D_α profiles with calculated connection lengths at the divertor target from the vacuum field line tracing, during the 3D field application with the coil current of $I_{3D} = 1$ kA. Note that lobe positions in heat flux and D_α profiles agree only approximately.

quickly responds to the applied 3D fields, i.e. the 'ear' in the pedestal region disappears in 15 ms after the application. The pedestal n_e profile stays reduced for $\Psi_N = 0.6$–0.8 during the whole period of 3D perturbation while the density continues to rise. The change in the pedestal T_e profile is not as significant as that in the density profile but is still measurable. Thus the ν_e^* profile is unchanged over time before and after the 3D field application. This is because the density and temperature changes offset each other (note that collisionality is proportional to n_e/T_e^2). The T_i profile shows a clear drop after the application in the region of $\Psi_N > 0.9$. The pedestal electron collisionality values ($\nu_e^* \sim 1$–2) during the heat flux profile splitting are comparable to the DIII-D required minimum value of $\nu_e^* > 0.5$ [13].

Figure 4 compares the lower divertor IR images before and after the application of $n = 3$ 3D field perturbation at $t = 400$ ms, along with the heat flux and D_α profiles. Figures in row (*a*) show that there is no (or little) strike point splitting at an early stage of the discharge ($t = 180$ ms). It is interesting to note that there are weak striations in the IR image even before the external magnetic perturbation ($t = 398$ ms, figure 4(*b*)). Both the heat flux and the D_α profiles significantly broadened compared with those in figure 4(*a*) with modest local peaks in the profile. These multiple peaks and valleys are characteristic of the lobe structure shown in figure 1(*b*). This suggests that the intrinsic error field can already produce observable strike point splitting. In fact, this 'intrinsic' strike point splitting starts to appear earlier during the discharge, at $t \sim 200$ ms, and is present for the remainder of the discharge. It is unclear whether the profile broadening observed along with the appearance of intrinsic strike point splitting was caused by the onset of intrinsic splitting, i.e. by the intrinsic error field, or whether the broadening was just due to the plasma evolution and the intrinsic splitting was simply accompanying it. Also, the intrinsic strike point splitting is not ubiquitous in NSTX and there are examples of no intrinsic splitting observed for the whole plasma duration for some discharges. The possible source of intrinsic error fields and the plasma conditions for the intrinsic splitting to occur are presently under detailed investigation. The application of 3D field perturbation augments this intrinsic splitting, making the
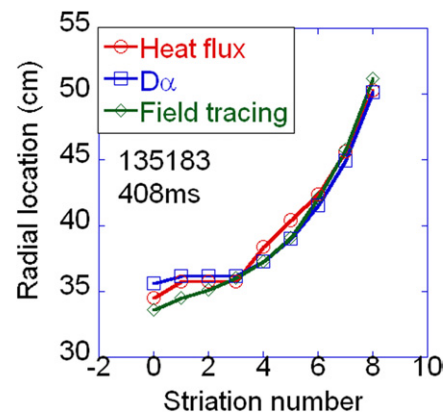

Figure 7. Radial position of lobes versus lobe number during the 3D field application. Data for 'field tracing' are from the connection length profile from the vacuum field line tracing, shown in figure 6.

striations brighter and clearer ($t = 432$ ms, figure 4(*c*)). As the plasma evolves, the striations become more pronounced ($t = 482$ ms, figure 4(*d*)). The width of heat flux and D_α profiles does not change significantly by the 'augmented' strike point splitting caused by the 3D field application (compare figures 4(*b*) and (*c*)). Note also that the peak heat and particle flux values are largely unchanged during the 3D field application. It is possible that the non-axisymmetric nature of the applied 3D field causes different profile widths and peak values at other toroidal locations than the one where the measurement is made at present. This possibility is planned to be investigated in the near future by rotating the applied 3D field during a single discharge. The response time of the 'augmented' strike point splitting to the 3D field application is as fast as 3–4 ms with the highest coil current of 1 kA. This is consistent with the measured time for a noticeable perturbation to develop through the vessel and the passive stabilizing plates, detected by the internal magnetic sensors, $\tau_{vessel} = 3$–4 ms.

The observed heat flux striation pattern was compared with the magnetic footprint from a vacuum field line following code, calculated for the toroidal angle of the IR camera. Figure 5 shows that the main characteristics of the heat flux profiles do follow the vacuum field line tracing results, both in
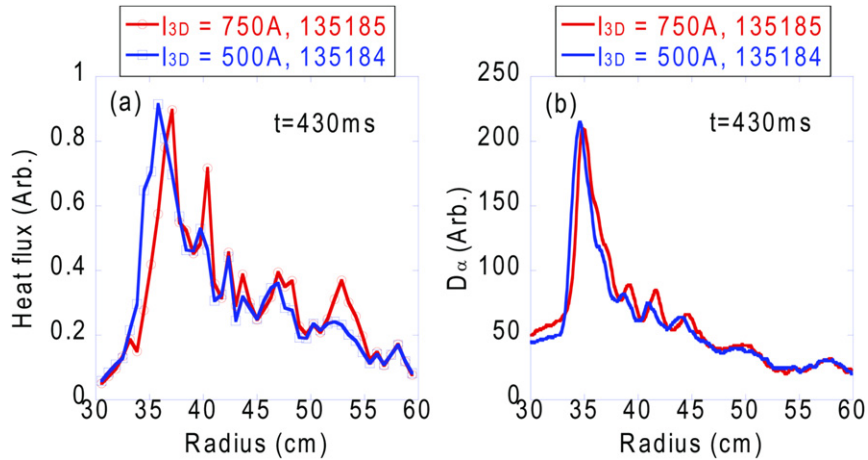
Figure 8. (*a*) Heat flux and (*b*) D_α profiles for two different 3D field coil currents, i.e. $I_{3D} = 0.75$ and 0.5 kA. The discharges are nominally identical except for the coil currents, for which heat flux and D_α measurements were carried out at the same time slice ($t = 430$ ms) after switching on the coils at $t = 400$ ms.

the number of observed striations and in the relative spacing of the peaks. Note, however, that the precise radial locations of the peak heat flux of the lobes slightly differ from those indicated by the vacuum field line tracing. A comparison of the heat flux and D_α profiles with the calculated connection lengths from the vacuum field line tracing is shown in figure 6. The long connection length field lines leave the stochastic area located inside the separatrix and therefore carry high electron temperature and density. It is thus expected that the location of peaks in the connection length profile and the heat flux and the D_α profiles agrees with each other. This is indeed observed in figure 6. Note that the local peaks between the heat and particle flux profiles differ by up to ~2 cm. The applied $n = 3$ magnetic perturbations are expected to produce the same radial lobe structures for both the IR and visible measurements because the diagnostics are spaced 120° apart. However, the contribution of the $n = 1$ and $n = 2$ components from the intrinsic error fields could result in the different locations for the observed peaks. In general, the heat and particle flux profiles could show different local peaks because they are correlated through convective heat transport, while conductive heat transport is thought to dominate the parallel heat transport in many NSTX discharges.

A closer look at the structure in the heat and particle flux profiles reveals that the radial separation between consecutive lobes increases with distance from the separatrix along the divertor plate (see figure 7). Note that lobes 1, 2 and 3 (the expected ones from the vacuum field line tracing, in reference to the radial location of the peak at the separatrix as the lobe number 0) appear as a combined local peak in the experimental heat flux and D_α profiles and therefore we have allocated the same value to the radial location for these three lobes in each of the heat flux and the D_α profiles. The magnitude of the peaks and valleys in the IR and D_α profiles was observed to increase with increasing coil current. On the other hand, the spacing between the lobes and the lobe widths is unaffected by the change in the coil current (figure 8). Note that the lower coil current, $I_{3D} = 0.5$ kA, is below the ELM triggering threshold value of $I_{3D} \sim 0.75$ kA. Heat flux and D_α profiles for $I_{3D} = 0.75$ kA were taken before the appearance of triggered ELMs.

4. Summary and conclusions

In this paper we have shown that the applied 3D field indeed modifies the heat and particle flux profiles in a manner consistent with vacuum field line tracing in NSTX H-mode plasmas. A weak splitting of strike points in both profiles is observed even before the application of 3D fields, possibly due to the intrinsic error fields, in these discharges (intrinsic strike point splitting is not a ubiquitous result in NSTX). This intrinsic strike point splitting appears to be augmented by the applied $n = 3$ fields. The measurement shows that the heat flux profile is very sensitive to both the intrinsic and the applied 3D field perturbations, forming multiple peaks radially separated on the divertor surface. The D_α profile, used as a proxy to the particle flux profile, also shows clear profile modification. The structures of split strike points for the heat flux and D_α profiles were found to be similar, both for the location and for the spacing. The amplitude of these structures was measured to increase with the amplitude of the 3D field coil current.

Acknowledgments

References

[1] Schaffer M.J., Menard J.E., Aldan M.P., Bialek J.M., Evans T.E. and Moyer R.A. 2008 *Nucl. Fusion* **48** 024004
[2] Snyder P.B., Wilson H.R., Osborne T.H. and Leonard A.W. 2004 *Plasma Phys. Control. Fusion* **46** A131
[3] Luxton J.L. 2002 *Nucl. Fusion* **42** 614–33

[4] Burrell K.H. *et al* 2005 *Plasma Phys. Control. Fusion* **47** B37–B52

[5] Evans T.E. *et al* 2006 *Nature Phys.* **2** 419–23

[6] Moyer R.A. *et al* 2005 *Phys. Plasmas* **12** 056119

[7] Evans T.E. *et al* 2008 *Nucl. Fusion* **48** 024002

[8] Ono M. *et al* 2000 *Nucl. Fusion* **40** 557

[9] Maingi R. *et al* 2009 *Phys. Rev. Lett.* **103** 075001

[10] Canik J.M. *et al* 2010 *Phys. Rev. Lett.* **104** 045001

[11] Canik J.M. *et al* 2010 *Nucl. Fusion* **50** 034012

[12] Evans T.E., Roeder R.K.W., Carter J.A., Rapoport B.I., Fenstermacher M.E. and Lasnier C.J. 2005 *J. Phys.: Conf. Ser.* **7** 174–90

[13] Jakubowski M.W. *et al* 2009 *Nucl. Fusion* **49** 095013

[14] Ahn J-W., Maingi R., Mastrovito D. and Roquemore A.L. 2010 *Rev. Sci. Instrum.* **81** 023501

[15] Herrmann A. *et al* 1995 *Plasma Phys. Control. Fusion* **37** 17

[16] Maingi R. *et al* 2003 *Nucl. Fusion* **43** 969

[17] Sabbagh S.A. *et al* 2006 *Phys. Rev. Lett.* **97** 045004

[18] Menard J.E. *et al* 2007 *Nucl. Fusion* **47** S645

[19] Mastrovito D., Maingi R., Kugel H.W. and Roquemore A.L. 2003 *Rev. Sci. Instrum.* **74** 5090

[20] Soukhanovskii V.A. *et al* 2003 *Rev. Sci. Instrum.* **74** 2094

[21] Kugel H.W. *et al* 2008 *Phys. Plasmas* **15** 056118